J Solid State Electrochem (2011) 15:2031–2039
DOI 10.1007/s10008-010-1228-0

ORIGINAL PAPER

Electrochemical kinetics of nanosized Ag and Ag_2O thin films prepared by radio frequency magnetron sputtering

Jian Xie · Nobuyuki Imanishi · Atsushi Hirano · Yashuo Takeda · Osamu Yamamoto · Xin-Bing Zhao · Gao-Shao Cao

Received: 3 August 2010 / Revised: 21 October 2010 / Accepted: 24 October 2010 / Published online: 7 November 2010

Abstract Ag and Ag_2O thin films have been prepared by radio frequency magnetron sputtering on Cu substrates and have been characterized by X-ray diffraction, scanning electron microscope and atomic force microscope. The electrochemical performance of the thin films has been studied by galvanostatic cycling and cyclic voltammetry. The potential dependence of Li-ion chemical diffusion coefficients, $\widetilde{D}_{Li}$, of the films has been determined by galvanostatic intermittent titration technique and electrochemical impedance spectroscopy. It is found that Li-ion chemical diffusion coefficients of the Ag film range from 10^{-16} to 3×10^{-14} cm^2s^{-1}. The Ag/Li_2O composite that is formed from Ag_2O after the first cycle exhibits higher $\widetilde{D}_{Li}$ values than the Ag film, especially at a low Li-intercalation content. The phase transitions in the two-phase region cause a significant decrease of chemical diffusion coefficients.

Keywords Thin film Li batteries · Ag/Ag_2O nano-grains · Chemical diffusion coefficient · Galvanostatic intermittent titration technique · Electrochemical impedance spectroscopy

J. Xie (✉) · X.-B. Zhao · G.-S. Cao
Department of Materials Science and Engineering, Zhejiang University,
Hangzhou 310027, China
e-mail: xiejian1977@zju.edu.cn

N. Imanishi · A. Hirano · Y. Takeda · O. Yamamoto
Department of Chemistry, Faculty of Engineering, Mie University,
1577 Kurimamachiya-cho,
Tsu, Mie 514-8507, Japan

Introduction

In the past decade, great attention has been paid to some Li-active metals, alloys, and compounds with high specific capacity, such as Sn [1–5], Sb [1, 5–9], Bi [10–13], In [14], Zn [11, 15, 16], and Ag [17–19] to replace the conventional carbon-based materials, aiming at high energy density application. Although these materials generally exhibited a high specific capacity, their long-term cycling stability, however, is unsatisfactory because of the large volume changes during alloying and de-alloying process. Therefore, the practical use of these anode materials in commercial Li-ion batteries is not realized yet. Recently, a renewed interest has been focused on the potential use of these high-capacity materials in thin-film microbatteries, due to the significantly decreased absolute volume changes when the thickness of thin films is reduced to micron scale or below. Promising cycling stability was achieved for some Sn, Sb, and Ag-based thin film cells [20–26].

Among the Li-active metals for thin-film microbatteries application, Ag received special interest because: firstly, it gives a high theoretical capacity of 790 $mAh\,g^{-1}$ when a Li_4Ag composition is formed; secondly, its alloying and de-alloying process occurs in a low potential range of 0–0.3 V, guaranteeing a high operating voltage in a full cell [27, 28]; thirdly, the cost of Ag becomes less important and volume change effect is minimized when made into thin-film form. Although Ag has a high electronic conductivity, Li-ion diffusion rate in the film should also be taken into consideration for high cell performance. It is, therefore, very important to determine the Li-ion chemical diffusion coefficients of Ag, in order

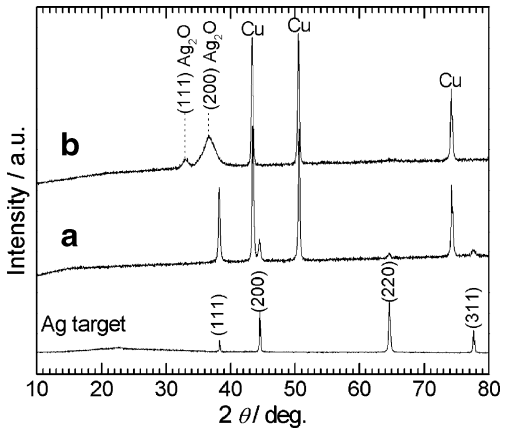

Fig. 1 XRD patterns of the films sputtered in *a* Ar and *b* Ar/O_2 (30% O_2) using Ag target

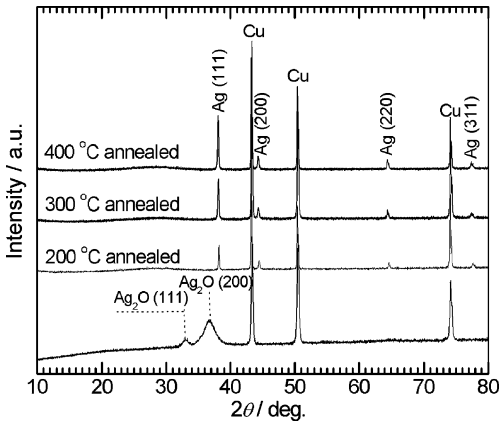

Fig. 3 XRD patterns of the Ag_2O films annealed at various temperatures

to clarify the intrinsic limiting factors of electrochemical performance of the cell. However, the detailed information of Li-ion diffusion kinetics in Ag is unavailable.

In this work, Ag thin films were prepared by radio frequency (RF) magnetron sputtering and the Li-ion chemical diffusion coefficients in the thin films were measured by galvanostatic intermittent titration technique (GITT) and electrochemical impedance spectroscopy (EIS). For comparison, Ag_2O thin films were also prepared and its Li-ion diffusion kinetics was also investigated.

Experimental

Ag and Ag_2O thin films (8×8 mm) were deposited on the polished Cu substrates (10×10 mm) by RF magnetron sputtering using an Ulvac SCOTT-C3. A silver foil was used as target. Thin films depositions were carried out for 10 min in pure Ar for Ag and in an Ar/O_2 mixture (30% O_2) for Ag_2O, with a working pressure of 0.4 Pa and a sputtering power of 20 W. The weight of the film was determined by weighing the substrate before and after sputtering using a precision balance. The crystallinity of the films was characterized by X-ray diffraction (XRD) using a RINT2000/PC diffractometer with $Cu-K_\alpha$ radiation. The surface and cross-sectional morphologies of the as-prepared films were observed by scanning electron microscope (SEM) using a Hitachi S-4800. The cross-sectional views of the Ag and Ag_2O electrodes at different charge and discharge states were also observed by SEM. In this case, somewhat thicker films were used for easy observation. To investigate the effect of temperature on the microstructure changes of the Ag_2O film, the as-deposited Ag_2O films were annealed at 200–400 °C for 30 min in Ar. The microstructures of the as-prepared and cycled Ag_2O films were also characterized by transmission electron microscopy (TEM) and selected area electron diffraction (SAED). The Raman spectroscopy of the Ag_2O film after the first full cycle was recorded using a LabRamHRUV instrument equipped with 15 mW He-Ne laser (632.8 nm). The Ag-to-O atomic ratio of the Ag_2O film was roughly estimated by energy dispersive X-ray (EDX).

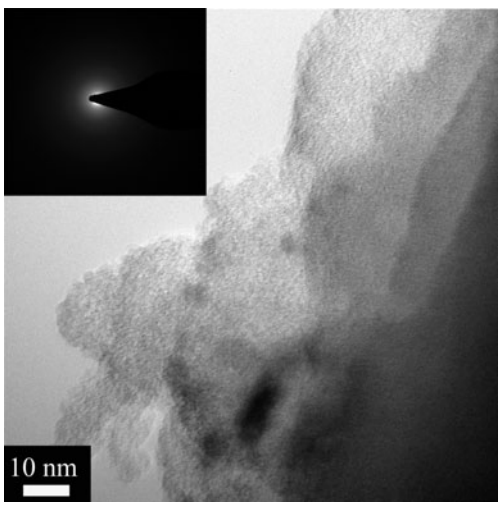

Fig. 2 TEM image and SAED pattern of the as-prepared Ag_2O film

Three-electrode beaker cells were used to evaluate the electrochemical performance of the thin films. The cells were assembled in an Ar-filled glove box using Li foils as both the counter and reference electrodes. The electrolyte used was 1 M $LiClO_4$ in a mixture of ethylene carbonate/diethyl carbonate (1:1 in volume). Galvanostatic cycling of the cells was carried out at 30 μA (46.9 $\mu A cm^{-2}$) between 0.01 and 1.5 V. Cyclic voltammetry (CV) measurements were performed between 0.01 and 1.5 V at a scanning rate of 1 $mV s^{-1}$ using a Solartron 1287 electrochemical interface. The CV plots were recorded after the first galvanostatic cycling. Li-ion chemical diffusion coefficients were measured by GITT and EIS methods after cycling the cells for three times. For GITT measurement, the cells were

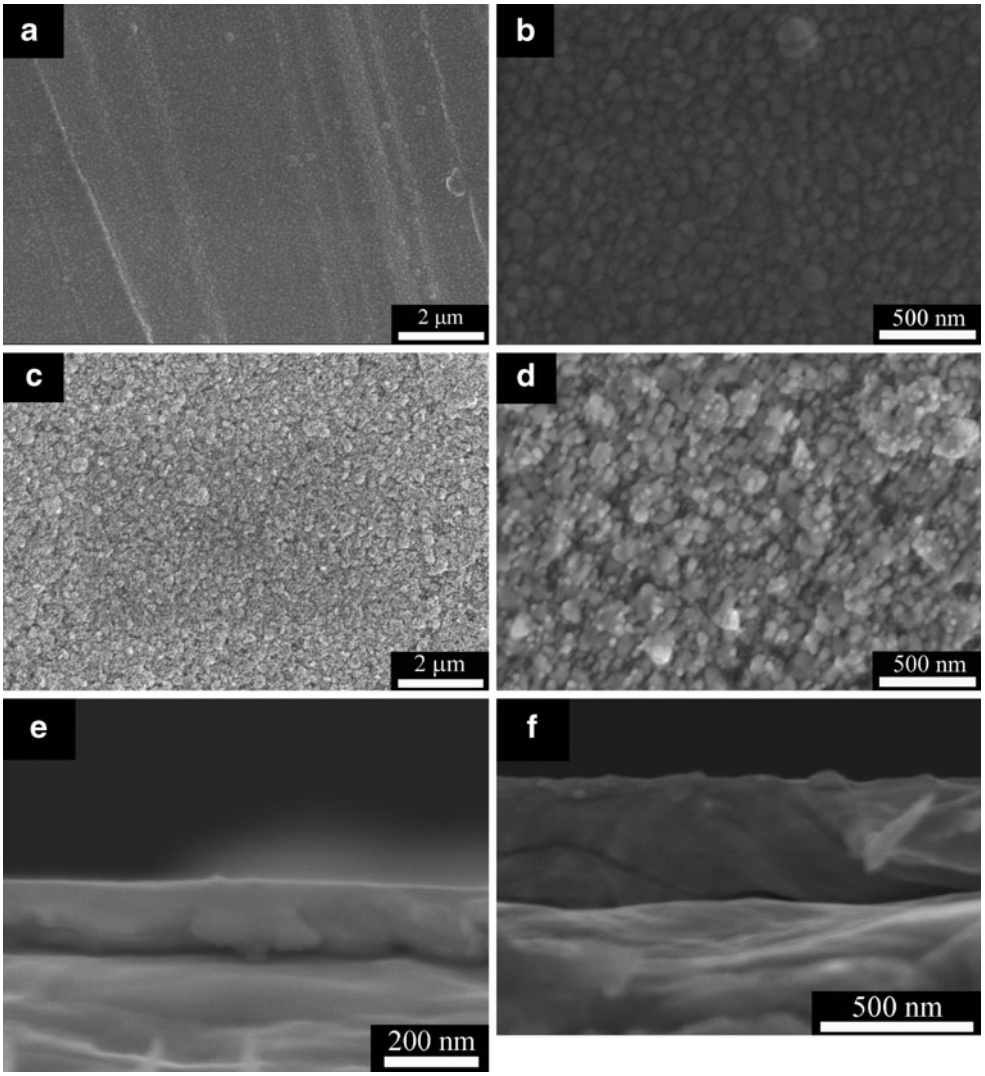

Fig. 4 SEM images of the Ag and Ag_2O thin films: **a**, **b** surface views of the Ag film, **c**, **d** surface views of the Ag_2O film, and **e**, **f** cross-section views of the Ag and Ag_2O films

discharged at 10 μA (15.6 $\mu A cm^{-2}$) for 20 min followed by an open circuit relaxation for 100 min. The procedure was continued until the cell potential reaches a given value. Due to the complex phase transitions upon Li-uptake, the lithiation process is rather sluggish at a low current density. Therefore, a relatively long current pulse is necessary to complete the whole titration process. EIS measurements were conducted by applying an AC signal of 10 mV amplitude over the frequency range from 1 MHz to 1 mHz using a Solartron 1287 electrochemical interface combined with a Solartron 1260 frequency response analyzer. All the electrochemical measurements were performed at 20 °C.

Results and discussion

Figure 1 shows the XRD patterns of the films sputtered in Ar and in an Ar/O_2 mixture (30% O_2). As seen in Fig. 1(a), well-crystallized Ag is formed when the sputtering was carried out in pure Ar without pre-heating the substrate. The self-generated temperature in the chamber is below 30 °C after the sputtering. For the preparation of crystalline Ag film by a spray pyrolysis method, a substrate pre-heating step was needed [29]. When the sputtering was performed in an Ar/O_2 mixture (30% O_2), the diffraction peaks are weak and broad as seen in Fig. 1(b), indicating poor crystallization of the Ag_2O film. Figure 2 shows the TEM image and SAED pattern of the as-prepared Ag_2O film. The rather diffuse and ill-defined diffraction rings indicate the poorly crystalline or amorphous nature of the Ag_2O film, in agreement with the XRD result. Figure 3 shows the XRD patterns of the Ag_2O films annealed at various temperatures. Note that the amorphous Ag_2O film undergoes thermal decomposition into crystallized Ag at a temperature as low as 200 °C in a short time of 30 min. This is one of the reasons for sputtering Ag_2O film at ambient temperature. The Ag-to-O atomic ratio of the as-prepared Ag_2O film is estimated to be 2:0.88 as analyzed by EDX.

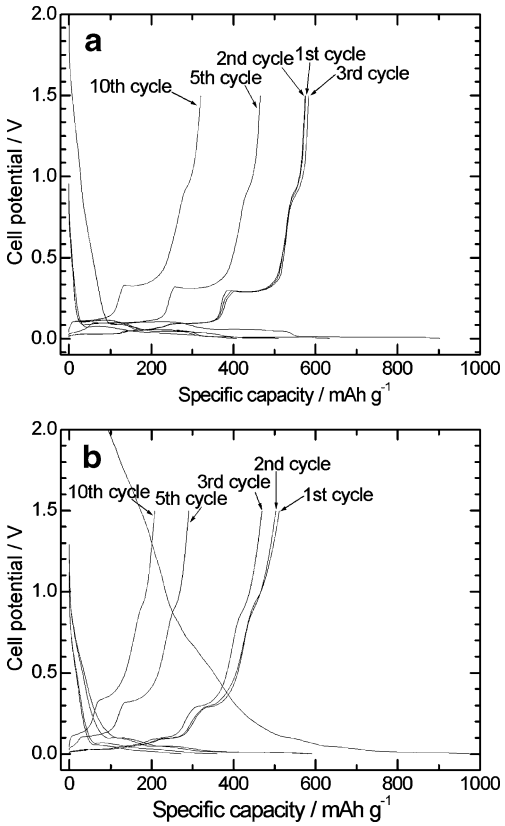

Fig. 5 Charge and discharge curves of the *a* Ag film and *b* the Ag/Li_2O composite at 30 μA (46.9 μAcm^{-2})

Figure 4 shows the SEM images of the as-prepared Ag and Ag_2O thin films. For the Ag film, its surface is smooth and crack free as seen in Fig. 4(a). High-magnification view indicates that the Ag film is composed of irregularly shaped grains with a size of around 100 nm, and the grain boundaries can be clearly distinguished as shown in Fig. 4(b). In contrast, the surface of the Ag_2O film is coarse and the Ag_2O grains exhibit a smaller size than Ag

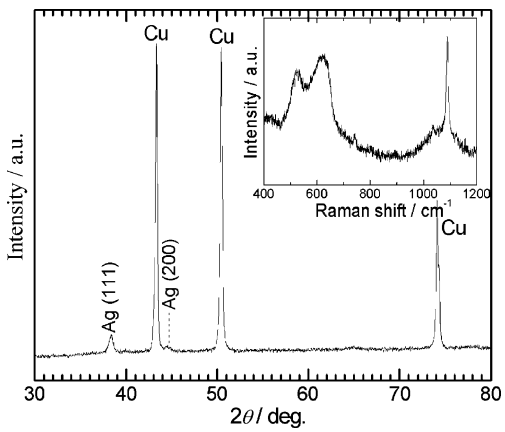

Fig. 6 XRD pattern of the Ag_2O electrode after the first full cycle. The inset shows the Raman spectroscopy of the electrode after the first cycle

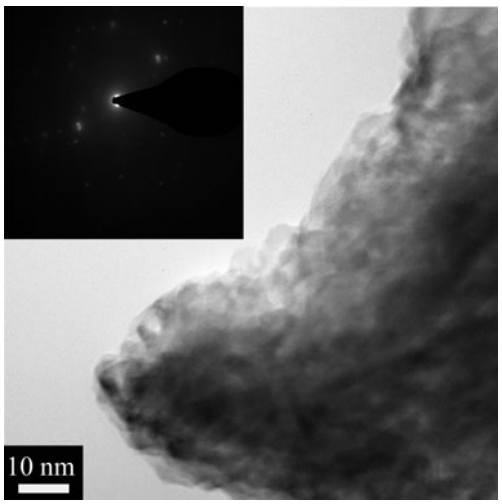

Fig. 7 TEM image and SAED pattern of the Ag_2O film after the first full cycle

grains without obvious grain boundaries as seen in Fig. 4(c) and (d). It should be noted that the nanostructure may only exist on the surface of the films caused possibly by the exposure of the film to the low-pressure sputtering chamber, and the films are generally compact and crack free as confirmed by the cross-section images in Fig. 4(e) and (f). The thicknesses of the Ag and Ag_2O films are estimated to be 0.16 and 0.44 μm, respectively.

Figure 5 shows the charge and discharge curves of the Ag and Ag_2O films at 30 μA (46.9 μAcm^{-2}). As seen in Fig. 5(a), the first discharge capacity of the Ag film reaches about 900 mAhg^{-1}. Note that unlike the subsequent discharge processes, the first discharge curve exhibits a sloping feature in the voltage range 2–0.1 V, which accounts for a capacity of about 100 mAhg^{-1}. This part of capacity is related to the formation of a solid electrolyte interface (SEI) layer caused by the reduction decomposition of the organic electrolyte at low electrode potentials. After the first cycle, both charge and discharge curves are almost overlapped. Because the electrolyte reduction occurs only

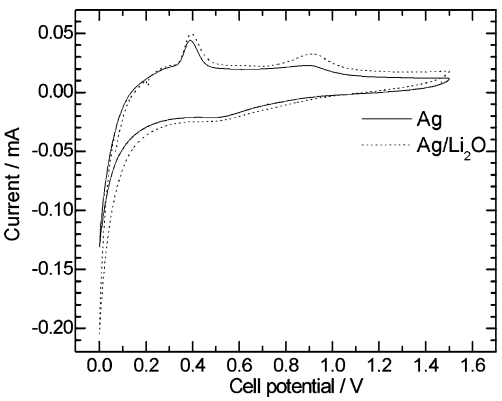

Fig. 8 CV plots of the Ag film and the Ag/Li_2O composite scanned at 1 mVs^{-1}

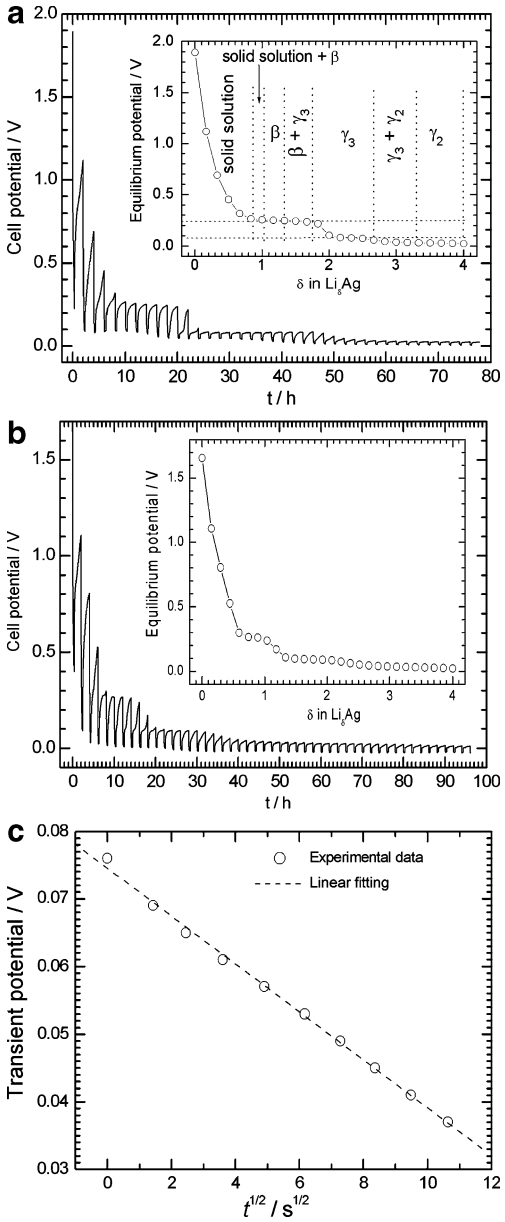

Fig. 9 GITT results of the Ag film and the Ag/Li_2O composite: (**a**) titration curve of the Ag film, the inset is the equilibrium potential vs. composition δ, (**b**) titration curve of the Ag/Li_2O composite, the inset is the equilibrium potential vs. composition δ, and (**c**) the transient potential vs. square root of the titration time $t^{1/2}$ for a single titration process at 0.076 V of the Ag film

in the first discharge process, it should not have significant influence on the measurement of the Li-ion diffusion coefficients. The discharge capacity of the as-deposited Ag film is 634 $mAh\,g^{-1}$ in the second cycle, which is higher than that of the nano-Ag electrode (with binder and conducting additive) [30], and comparable with that of the well-crystallized thin-film electrode [29] at similar current densities.

It is clear that successive plateaus are evolved during charge and discharge. Ex situ XRD results showed that a

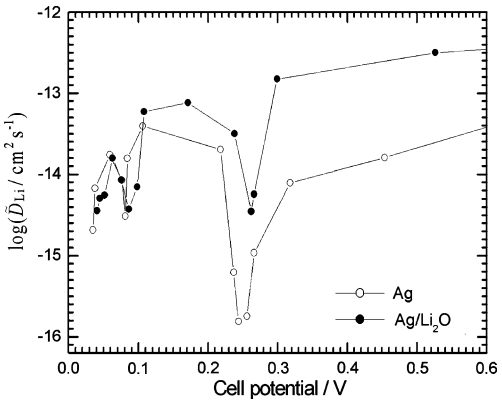

Fig. 10 Comparison of Li-ion chemical diffusion coefficients between the Ag film and the Ag/Li_2O composite using GITT

series of Li-Ag intermediate phases, such as β (LiAg), γ_3 (Li_9Ag_4), and γ_2 ($Li_{10}Ag_3$), can be formed during the electrochemical lithiation process [28, 30]. The plateau in the charge and discharge curves is related to the two-phase mixture, while in the single phase region, the potential depends on the amount of Li intercalation.

As shown in Fig. 5(b), for the Ag_2O film, a large irreversible capacity is observed in the first cycle. It is suggested that the irreversible capacity is attributed to the irreversible decomposition of Ag_2O upon Li-uptake to produce Li_2O and Ag and the formation of SEI layer. Figure 6 shows the XRD patterns of the Ag_2O electrode after the first full cycle. It is obvious that Ag is formed without the recovery of Ag_2O. However, Li_2O is not detected in the XRD patterns because it may be in the form of nanosized grains [31]. Raman spectroscopy instead is used to check whether Li_2O was formed during the first cycle as shown in the inset of Fig. 6. The bands at about 520, 630, and 1,100 cm^{-1} clearly indicate the presence of Li_2O [32]. The Ag_2O electrode after the first full cycle was also characterized by TEM and SAED as indicated in Fig. 7. The ill-defined, irregularly scattered diffraction dots imply that the Ag grains converted from Ag_2O are partly crystallized, in consistent with the XRD observation. According to the above results, the Ag_2O film has been converted into Ag and Li_2O matrix after the first cycle. Therefore, Ag/Li_2O composite instead of Ag_2O is used in the following sections. Compared with the Ag film, the Ag/Li_2O composite exhibits undistinguishable separation of the potential plateaus, which may be due to the poor crystallization of the Ag_2O. It should be stressed that the cycling stability of both the Ag film and Ag/Li_2O composite is not satisfactory. Rapid capacity fade can be seen after repeated cycling. Figure 8 shows the CV plots of the electrode after the first charge and discharge cycle. The similarity of the plots between the two electrodes indicates that they exhibit similar lithiation/de-lithiation mechanism after the first cycle.

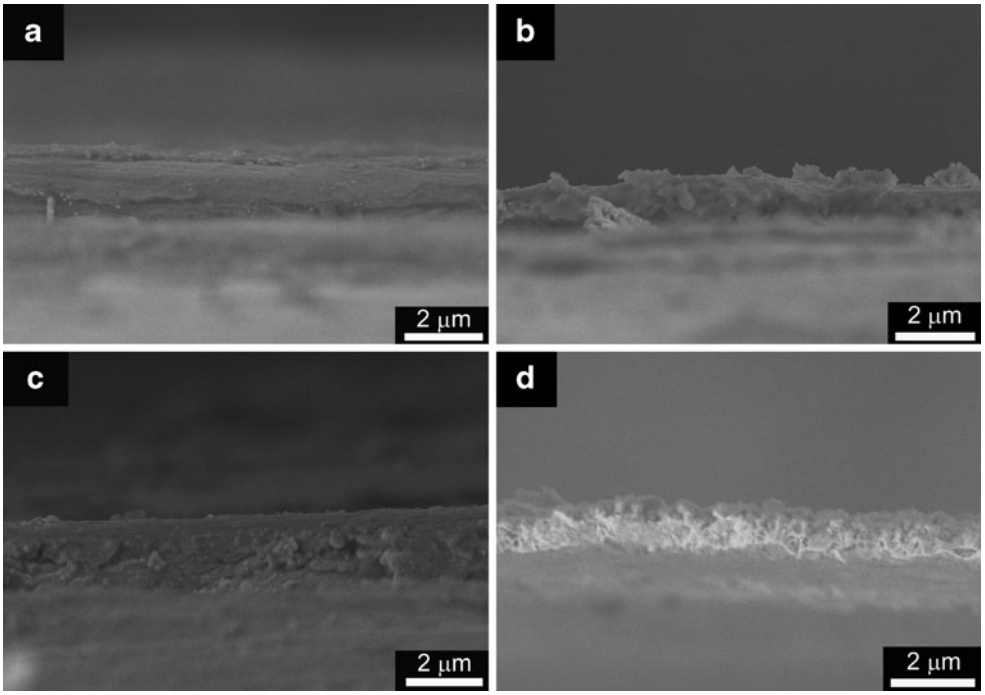

Fig. 11 Cross-sectional images of the Ag electrodes after the first **a** discharge and **b** charge process and the Ag/Li_2O electrode after the first **c** discharge and **d** charge process

Compared with the composite electrode, thin-film electrode is more suitable to characterize Li-ion diffusion kinetics since it is conducting additive and binder free and has uniform microstructure. GITT is a useful tool for the determination of the chemical diffusion coefficients. By solving the Fick's equation, the formula that calculates the $\widetilde{D}_{Li}$ values is written as [33]:

$$\widetilde{D}_{Li} = \frac{4}{\pi}\left(I_0 \frac{V_m}{FS}\right)^2 \left(\frac{dE}{d\delta} \Big/ \frac{dE}{dt^{1/2}}\right)^2, t \ll L^2/\widetilde{D}_{Li} \quad (1)$$

where $\widetilde{D}_{Li}$ ($cm^2 s^{-1}$), V_m ($cm^3 mol^{-1}$), F ($C mol^{-1}$), I_0 (A), S (cm^2), and L (cm) denote the Li-ion chemical diffusion coefficient, the molar volume of Ag (or Ag/Li_2O), the Faraday's constant, the applied current, the surface area of the electrode, and the thickness of the film, respectively. $dE/d\delta$ is the slope of the titration curve at each composition δ. The titration was stopped at a composition close to Li_4Ag. Figure 9(a) and (b) show typical GITT curves of the Ag film and the Ag/Li_2O composite measured by charging the cell at 10 μA (15.6 $\mu A cm^{-2}$) for 20 min followed by an open circuit relaxation for 100 min. The equilibrium potential recorded at the end of each relaxation as a function of the composition δ is plotted in the insets of Fig. 9(a) and (b), from which $dE/d\delta$ can be obtained. According to the ex situ XRD results [28, 30] and the Li-Ag binary phase diagram [30], the relationship between the phase transition and composition is also given in the inset of Fig. 9(a). Figure 9(c) shows the variation of the transient potential for a single titration at 0.076 V for the Ag film. Note that the potential exhibits a linear relationship with $t^{1/2}$ in a short time from which $dE/dt^{1/2}$ in Eq. (1) can be determined for each titration.

Figure 10 shows the chemical diffusion coefficients, $\widetilde{D}_{Li}$, as a function of cell potential by GITT. The $\widetilde{D}_{Li}$ values of the Ag film and the Ag/Li_2O composite are in the range of 10^{-16} to 3×10^{-14} and 3×10^{-15} to 3×10^{-13} $cm^2 s^{-1}$, respectively. It seems that the Ag/Li_2O composite gives higher $\widetilde{D}_{Li}$ values than the Ag film at low Li-intercalation degree. This may be ascribed mainly to its poor crystallization feature and its unique microstructure, that is, Li_xAg in the Li_2O matrix as mentioned above. In addition, as indicated in Fig. 11, the electrodes undergo microstructural changes upon charge and discharge cycling. For the Ag electrode, it seems that the dense structure is maintained after cycling as shown in Fig. 11(a) and (b). For the Ag/Li_2O electrode, however, the grain size is relatively small and the grains are loosely stacked with a porous structure after cycling as seen in Fig. 11(c) and (d). This microstructure that may be formed by the phase separation of Ag and Li_2O facilitates the rapid Li-ion diffusion. At a deep discharge state, however, the two films exhibit similar $\widetilde{D}_{Li}$ values, which may be due to the similar Li-Li coulombic repulsion effect at a high Li concentration. On the whole, the introduction of oxygen in Ag lattice increases its Li-ion diffusion rate. It is favorable because the deposition conditions for the Ag_2O film are compatible with those for amorphous cathode films [34, 35], suggesting that the fabrication process of the thin-film microbatteries can be simplified.

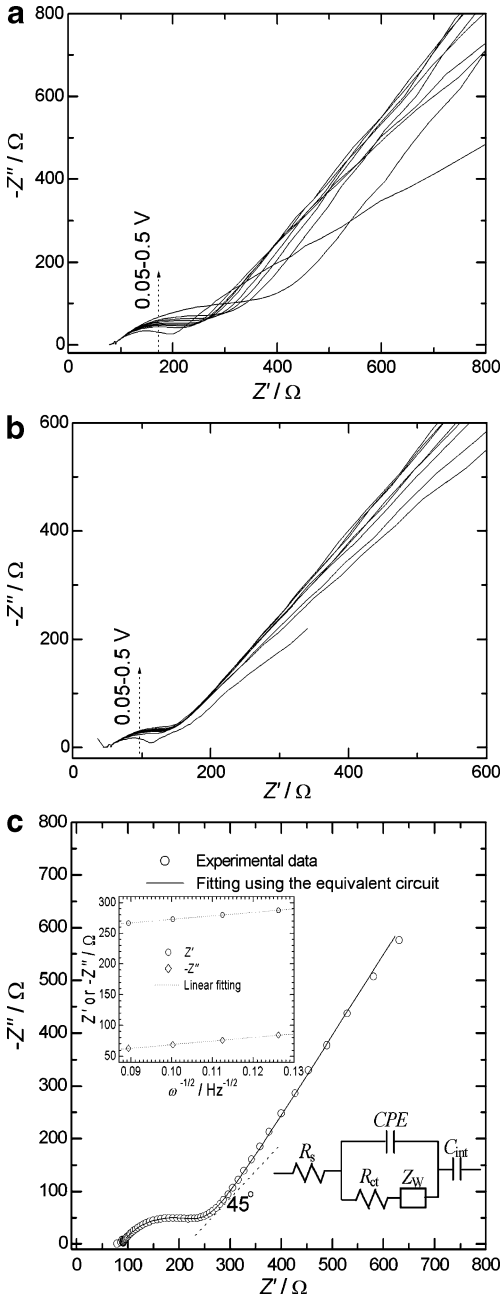

Fig. 12 EIS results of the Ag film and the Ag/Li_2O composite: **a** Nyquist plots of the Ag film at various cell potentials, **b** Nyquist plots of the Ag/Li_2O composite at various cell potentials, and **c** a typical Nyquist plot of the Ag film at 0.1 V, the insets are equivalent circuit and relationship between Z' or $-Z''$ and $\omega^{-1/2}$

Two minima of $\widetilde{D}_{Li}$ appear at the potentials around 0.25 and 0.1 V as seen in Fig. 10, which correspond to the potential plateaus in the insets of Fig. 9(a) and (b). Although the exact mechanism for the appearance of the minima $\widetilde{D}_{Li}$ values is unclear due to the complex phase transition upon Li interaction, it may be related to the formation of the two Li-rich phases γ_3 (Li_9Ag_4) and γ_2 ($Li_{10}Ag_3$). It should be stressed that GITT method cannot

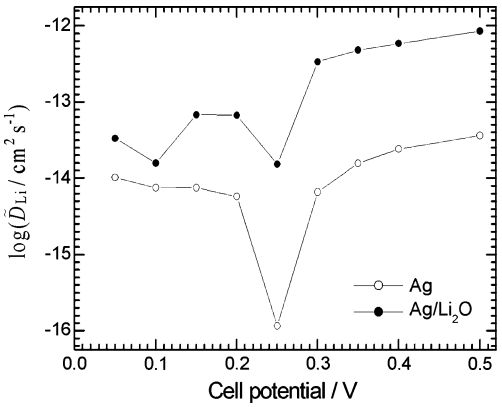

Fig. 13 Comparison of Li-ion chemical diffusion coefficients between the Ag film and the Ag/Li_2O composite using EIS

give reliable $\widetilde{D}_{Li}$ values since the potential is independent of the composition in the two-phase region, where $dE/d\delta$ is close to zero. Therefore, the $\widetilde{D}_{Li}$ values in the two-phase region can only be considered as apparent values. From Fig. 9(b), it seems that the amorphization or part crystallization makes the potential plateaus exhibit a sloping feature instead of a straight line parallel to the x axis, implying that the phase transition becomes blurred. Recent studies showed that particle size also has a great effect on the reaction mechanism and phases involved upon Li insertion [36–38]. With the decreasing particle size, a sloped plateau will appear in the two-phase regions. Therefore, the smaller grain size of the Ag/Li_2O composite may also contribute to the sloping potential plateaus.

EIS is another powerful tool to identify the kinetics of Li insertion/extraction into/from the electrode. In this work, it was also used to evaluate the potential dependence of the Li-ion chemical diffusion coefficient. Prior to the EIS measurements, the cell was also activated by galvanostatic cycling. Figure 12(a) and (b) show the Nyquist plots of the Ag film and Ag/Li_2O composite polarized at various cell potentials. Note that for both the electrodes, the diameter of semicircle in the Nyquist plot is on the decrease during Li-insertion process. Figure 12(c) gives a typical Nyquist plot polarized at 0.1 V, which consists of a semicircle in the high-frequency region, a straight line with a slope of approximately 45° in the medium frequency region, and a steeper straight line in the low-frequency region. The high-frequency semicircle can be attributed to a charge transfer process, the straight line of 45° slope is attributed to the Warburg diffusion of Li-ions in the Ag bulk, and the steeper straight line corresponds to the onset of the finite length diffusion. The Nyquist plot can be fitted by an equivalent circuit shown in the inset of Fig. 12(c), where R_s is the ohm resistance, R_{ct} and CPE represent the charge transfer resistance and the corresponding constant phase element, respectively, Z_w is the Warburg resistance, and C_{int} is the

intercalation capacitance. Note that in the Warburg region, a linear dependence of Z' or $-Z''$ on $\omega^{-1/2}$ (ω is the angular frequency) is observed, with the slope of the fitting line as Warburg factor σ. The $\widetilde{D}_{\mathrm{Li}}$ values can be calculated using the following equation [39]:

$$\widetilde{D}_{\mathrm{Li}} = \frac{1}{2}\left[\left(\frac{V_{\mathrm{m}}}{FS\sigma}\right)\left(\frac{\mathrm{d}E}{\mathrm{d}\delta}\right)\right]^2 \quad (2)$$

where V_{m}, F, S, and $\mathrm{d}E/\mathrm{d}\delta$ have the same meaning as in Eq. (1), σ ($\Omega\mathrm{Hz}^{1/2}$) is the Warburg factor, and $\mathrm{d}E/\mathrm{d}\delta$ can also be obtained from Fig. 9.

Figure 13 shows the Li-ion chemical diffusion coefficients at various cell potentials by EIS. The $\widetilde{D}_{\mathrm{Li}}$ values of the Ag film and the Ag/Li_2O composite by EIS are in the range of 10^{-16} to 3×10^{-14} and 10^{-14} to 10^{-12} cm^2s^{-1}, respectively, agreeing generally with those by GITT. Two minima of $\widetilde{D}_{\mathrm{Li}}$ values are also evident at around 0.25 and 0.1 V using EIS method, in consistent with the GITT result. Again, in the two-phase region the $\widetilde{D}_{\mathrm{Li}}$ values are only regarded as the apparent values using EIS method. It should be noted that the $\widetilde{D}_{\mathrm{Li}}$ values of the Ag film and the Ag/Li_2O composite are smaller compared with those of some Sb- and Sn-based composite electrodes measured also by GITT or EIS [40–43]. The $\widetilde{D}_{\mathrm{Li}}$ values of the Ag film and the Ag/Li_2O composite are also smaller than that of $Li_4Ti_5O_{12}$ thin film measured by EIS [44]. The $Sn_{1-x}Si_xO_2$ based composite electrode, which also contains Li_2O after initial cycling, exhibited $\widetilde{D}_{\mathrm{Li}}$ values of 10^{-10}–10^{-8} cm^2s^{-1} measured by GITT method [45], also higher than our Ag/Li_2O electrode. The low $\widetilde{D}_{\mathrm{Li}}$ values of the Ag film and the Ag/Li_2O composite can be attributed to their complicated phase transformation upon Li-absorption and the compact thin-film structure. However, the intrinsic diffusion kinetics can be reflected by the thin-film electrodes that are binder and conductive additive free.

Conclusion

Ag and Ag_2O thin films were prepared by RF magnetron sputtering on the Cu substrates. The as-deposited Ag film exhibits a well-crystallized structure, while the as-deposited Ag_2O shows a poor crystallization. The Li-ion diffusion coefficients of the Ag film and the Ag/Li_2O composite were determined by GITT and EIS. The Ag film demonstrates $\widetilde{D}_{\mathrm{Li}}$ values ranging from 10^{-16} to 3×10^{-14} cm^2s^{-1} by both GITT and EIS methods. The low $\widetilde{D}_{\mathrm{Li}}$ values may be caused mainly by the complex phase transition during the Li-intercalation process. The Ag/Li_2O composite demonstrates $\widetilde{D}_{\mathrm{Li}}$ values of 3×10^{-15}–3×10^{-13} cm^2s^{-1} by GITT and 10^{-14}–10^{-12} cm^2s^{-1} by EIS. The increase of $\widetilde{D}_{\mathrm{Li}}$ values of the Ag/Li_2O composite compared with Ag is caused by its amorphous feature, small grain size, loosely stacked grains, and unique microstructure, namely, Li_xAg in the Li_2O matrix. Two minima of $\widetilde{D}_{\mathrm{Li}}$ values can be observed in the two-phase region, which can only be regarded as the apparent chemical diffusion coefficients due to the phase transitions. Further work should be undertaken to optimize the microstructure to increase the Li-ion diffusion kinetics aiming at a high cell performance.

Acknowledgments This research work was carried out under a collaboration program of Mie University and Genesis Research Institute, Nagoya, Japan. We also thank the support of Zijin Program of Zhejiang University and by the Fundamental Research Funds for the Central Universities (Program No. 2010QNA4003).

References

1. Yang J, Winter M, Besenhard JO (1996) Solid State Ionics 90:281–287
2. Idota Y, Kobota T, Matsufuji A, Maekawa Y, Miyasaka T (1997) Science 276:1395–1397
3. Kepler KD, Vaughey JT, Thackeray MM (1999) Electrochem Solid-State Lett 2:307–309
4. Mao O, Dunlap RA, Dahn JR (1999) J Electrochem Soc 146:405–413
5. Larcher D, Beaulieu LY, Mao O, George AE, Dahn JR (2000) J Electrochem Soc 147:1703–1708
6. Monconduit L, Jumas JC, Alcántara R, Tirado JL, Pérez Vicente C (2002) J Power Sources 107:74–79
7. Santos Peña J, Cuart Pascual J, Caballero A, Morales J, Sánchez L (2004) J Solid State Chem 177:2920–2927
8. Stjerndahl M, Bryngelsson H, Gustafsson T, Vaughey JT, Thackeray MM, Edström K (2007) Electrochim Acta 52:4947–4955
9. Morcrette M, Larcher D, Tarascon JM, Edström K, Vaughey JT, Thackeray MM (2007) Electrochim Acta 52:5339–5345
10. Crosnier O, Brousse T, Devaux X, Fragnaud P, Schleich DM (2001) J Power Sources 94:169–174
11. Zhao XB, Cao GS, Lv CP, Zhang LJ, Hu SH, Zhu TJ, Zhou BC (2001) J Alloys Compd 315:265–269
12. Crosnier O, Devaux X, Brousse T, Fragnaud P, Schleich DM (2001) J Power Sources 97–98:188–190
13. Pérez-Flores JC, Kuhn A, García-Alvarado F (2008) J Power Sources 182:365–369
14. Johnson CS, Vaughey JT, Thackeray MM, Sarakonsri T, Hackney SA, Fransson L, Edström K, Thomas JO (2000) Electrochem Commun 2:595–600
15. Zhao XB, Cao GS (2001) Electrochim Acta 46:891–896
16. Hwang H, Kim MG, Kim Y, Martin SW, Cho J (2007) J Mater Chem 17:3161–3166
17. Wachtler M, Winter M, Besenhard JO (2002) J Power Sources 105:151–160
18. Vaughey JT, Fransson L, Swinger HA, Edström K, Thackeray MM (2003) J Power Sources 119–121:64–68
19. Yin JT, Wada M, Tanase S, Sakai T (2004) J Electrochem Soc 151:A867–A872
20. Pralong V, Leriche JB, Beaudoin B, Naudin E, Morcrette M, Tarascon JM (2004) Solid State Ionics 166:295–305
21. Mukaibo H, Momma T, Mohamedi M, Osaka T (2005) J Electrochem Soc 152:A560–A565
22. Xue MZ, Fu ZW (2006) Electrochem Commun 8:1250–1256

23. Hu RZ, Zhang L, Liu X, Zeng MQ, Zhu M (2008) Electrochem Commun 10:1109–1112
24. Hu RZ, Zeng MQ, Zhu M (2009) Electrochim Acta 54:2843–2850
25. Kim YL, Lee SJ, Baik HK, Lee SM (2003) J Power Sources 119–121:106–109
26. Xue MZ, Cheng SC, Yao J, Fu ZW (2006) Electrochim Acta 51:3287–3291
27. Kim HS, Cho WI, Cho BW, Ju JB (2002) J Power Sources 107:133–137
28. Taillades G, Sarradin J (2004) J Power Sources 125:199–205
29. Morales J, Sánchez L, Martín F, Ramos-Barrado JR, Sánchez M (2004) J Electrochem Soc 151:A151–A157
30. Park CM, Jung H, Sohn HJ (2009) Electrochem Solid-State Lett 12:A171–A175
31. Liu HC, Yen SK (2007) J Power Sources 166:478–484
32. Gejke C, Zanghellini E, Börjesson L, Fransson L, Edström K (2001) J Phys Chem Solids 62:1213–1218
33. Weppner W, Huggins RA (1977) J Electrochem Soc 124:1569–1578
34. Xie J, Imanishi N, Zhang T, Hirano A, Takeda Y, Yamamoto O (2010) J Power Sources 195:5780–5783
35. Xie J, Imanishi N, Zhang T, Hirano A, Takeda Y, Yamamoto O, Cao GS, Zhao XB (2010) Electrochim Acta 55:5440–5445
36. Wagemaker M, Borghols WJH, Mulder FM (2007) J Am Chem Soc 129:4323–4327
37. Muñoz-Rojas D, Casas-Cabanas M, Baudrin E (2009) Solid State Ionics 180:308–313
38. Muñoz-Rojas D, Casas-Cabanas M, Baudrin E (2009) Solid State Ionics 181:536–544
39. Ho C, Raistrick ID, Huggins RA (1980) J Electrochem Soc 127:345–350
40. Besenhard JO, Wachtler M, Winter M, Andreaus R, Rom I, Sitte W (1999) J Power Sources 81–82:268–272
41. Zhang LJ, Zhao XB, Jiang XB, Lv CP, Cao GS (2001) J Power Sources 94:92–96
42. Xie J, Zhao XB, Cao GS, Su SF (2005) J Electrochem Soc 152: A601–A606
43. Sreeraj P, Kaskhedikar NA, Wiemhöfer HD, Maier J, Pöttgen R (2010) Solid State Ionics 181:59–63
44. Rho YH, Kanamura K (2004) J Solid State Chem 177:2094–2100
45. Huang H, Kelder EM, Chen L, Schoonman J (1999) J Power Sources 81:362–367